Experiments in Fluids (2006) 41: 213–225
DOI 10.1007/s00348-006-0172-3

RESEARCH ARTICLE

C. Poelma · W. B. Dickson · M. H. Dickinson

Time-resolved reconstruction of the full velocity field around a dynamically-scaled flapping wing

Received: 25 November 2005 / Revised: 25 May 2006 / Accepted: 27 May 2006 / Published online: 6 July 2006
© Springer-Verlag 2006

Abstract The understanding of the physics of flapping flight has long been limited due to the obvious experimental difficulties in studying the flow field around real insects. In this study the time-dependent three-dimensional velocity field around a flapping wing was measured quantitatively for the first time. This was done using a dynamically-scaled wing moving in mineral oil in a pattern based on the kinematics obtained from real insects. The periodic flow is very reproducible, due to the relatively low Reynolds number and precise control of the wing. This repeatability was used to reconstruct the full evolving flow field around the wing from separate stereoscopic particle image velocimetry measurements for a number of spanwise planes and time steps. Typical results for two cases (an impulsive start and a simplified flapping pattern) are reported. Visualizations of the obtained data confirm the general picture of the leading-edge vortex that has been reported in recent publications, but allow a refinement of the detailed structure: rather than a single strand of vorticity, we find a stable pair of counter-rotating structures. We show that the data can also be used for quantitative studies, such as lift and drag prediction.

1 Introduction

Insects are capable of remarkable aerial acrobatics, which challenge our current understanding of unsteady aerodynamics. Insect wings operate in a Reynolds number range between 10^2 and 10^4, which complicates mathematical analysis and numerical studies (Wang 2005). In addition, experimental studies are hampered by the small scale and high flapping frequencies of real insects. Only recently, quantitative particle image velocimetry (PIV) experiments have been successfully reported on tethered insects of relatively large species, such as *Manduca sexta* (tobacco hawkmoth) and *Schistocerca gregaria* (desert locust), see Bomphrey et al. (2006a, b). A large number of open questions remain, however: some of them are mainly biological in nature, but many are relevant for general problems involving unsteady fluid–structure interaction.

Even the apparently very basic question of the general flow topology of flapping flight in insects and birds is an active topic of research (Bomphrey et al. 2005; Von Ellenrieder et al. 2003; Spedding et al. 2003; Hedenström et al. 2006). In recent years, visualizations using relatively large insects and scaled models have shed light on the structure of the flow dynamics. A number of mechanisms have been identified that may account for the forces that are generated by flapping wings (Ellington et al. 1996; Dickinson et al. 1999). These forces are significantly higher than those observed for 'conventional' translating wings (Sane and Dickinson 2002)—a discrepancy that can be attributed to unsteady fluid phenomena. One of the most striking examples of the latter is the development of a stable leading-edge vortex (LEV). In contrast to a linearly translating wing, the leading-edge vortex does not shed on a revolving wing during the stroke; see Fig. 1 for a schematic illustration of the LEV, visualizations can be found in e.g., work by Usherwood and Ellington (2002) and Birch and Dickinson (2001).

In this study, we analyze the flow field around a flapping wing, with a focus on the development and stability of the leading-edge vortex. In order to overcome the practical problems involved in measuring the flow field around real insects, a dynamically-scaled robotic wing submerged in mineral oil was used. The

C. Poelma · W. B. Dickson · M. H. Dickinson
Bioengineering, California Institute of Technology,
1200 East California Blvd, mail code 138-78,
Pasadena, CA 91101, USA
Tel.: +1-626-3955775

Present address: C. Poelma (✉)
Laboratory for Aero and Hydrodynamics,
Delft University of Technology,
Leeghwaterstraat 21, 2628 CA Delft, The Netherlands
E-mail: c.poelma@tudelft.nl
Tel.: +31-15-2782620

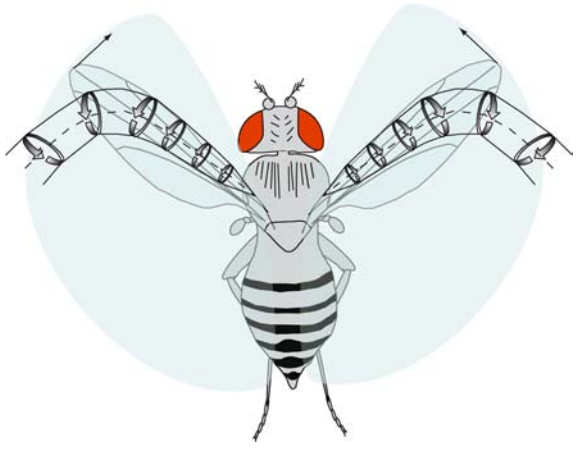

Fig. 1 Schematic illustration of the leading-edge vortex on the wings of a *Drosophila melanogaster* (*top view*). The *shaded area* represents the area swept by the wing

characteristics of this robotic wing are based on a fruit fly, *Drosophila melanogaster*. The dynamic scaling allows an increase in length and time scales (from 3 mm and 200 Hz to 25 cm and 1/6 Hz, respectively), while retaining the same Reynolds and Strouhal number and thus the same flow regime. The more convenient time and length scale make detailed PIV measurements feasible.

Due to the high repeatability of the flow, it is possible to reconstruct the entire flow field from separate measurements at different locations and temporal positions in the stroke cycle. This allows us to reveal the complete, transient three-dimensional flow around a flapping wing for the first time. Earlier work using PIV was predominantly done in either a single plane or a small number spanwise locations. For instance, Birch and Dickinson (2003) reconstructed the time series of the flow field at a single spanwise location. In the work of Birch et al. (2004), the spatial structure of the flow at a single instance during the flapping cycle was reconstructed from several spanwise planes. In the current study, we combined these two approaches to obtain the transient three-dimensional flow field. By utilizing a stereoscopic set-up, we were also able to obtain all three velocity (and vorticity) components.

The data obtained in this study can help link the well-studied field of 'classical' airfoil theory (Kutta–Joukowsky theorem, etc.) and the more empirical approach of current quasi-steady models of flapping flight. An example of the latter is the blade element approach (Sane and Dickinson 2002). In this approach, the total lift force generated by a wing is the sum of the contribution of a range of segments ('blade elements'). The contribution of these elements is calculated with relationships that are rooted in classical translating airfoil theory, but which are corrected using empirical constants for unsteady and three-dimensional effects. These constants are usually obtained from force measurements using revolving wings. While this approach gives reasonably good results, more insight in the fluid dynamics of flapping wings can hopefully also improve the underpinning physics of the measured force coefficients.

2 Experimental methods

2.1 Facility and scaled model wing

The experiments were performed using a facility described earlier (Birch and Dickinson 2001, 2003). The apparatus consisted of a dynamically-scaled robotic wing suspended in a large ($1 \times 1.5 \times 3$ m^3) rectangular tank filled with mineral oil (see Fig. 2). Computer-controlled servo motors controlled the wing accurately with respect to four degrees of freedom: wing rotation (i.e., angle-of-attack α, with $\alpha = 0°$ indicating a horizontal wing), stroke rotation (ϕ), stroke plane deviation (ζ) and linear translation (z). Using these parameters, the wing could perform the same movements as the wings of a real insect, either in hovering or forward flight. The prescribed wing kinematics will be described in a following section.

The wing was cut in the planform shape of a *Drosophila* wing from a 2.25-mm thick clear acrylic sheet. The maximum chord length of the wing was 10 cm. The distance L from point-of-rotation (o) to the wing tip was 25 cm, but the first 7 cm were taken up by a gear box and a force sensor (see Fig. 2, *right*). This force sensor could measure forces perpendicular and parallel to the wing (i.e., lift and drag) during the fluid velocity measurements. The mineral oil that was used has a density of 0.88 kg/m^3 and a kinematic viscosity of 115×10^{-6} m^2/s (Chevron 'Superla'). At a typical angular velocity of $(3/8)\pi$ rad/s, equivalent to a tip velocity of 0.29 m/s, this lead to a maximum chord length based Reynolds number of $Re = cU_{\text{tip}}/\nu = 256$, similar to a real *Drosophila*.[1]

The Reynolds number is not the only dimensionless number that is relevant in flapping flight. Since the flow is unsteady, an additional dimensionless parameter must be considered: the Strouhal number. This number compares a typical time scale of the fluid dynamics with a time scale describing some kind of internal or external cycle (Taylor et al. 2003). The latter is linked to the periodic vortex shedding from an object. This shedding is usually the result of a mean flow past an object. However, the current study deals with hovering flight, so there is no mean flow. Most of the vorticity remains attached throughout the stroke and the majority of shedding phenomena result from wing pronation and supination. This means that the dominating time scale

[1] It should be noted that there are alternative definitions in the literature for the Reynolds number of a flapping wing (e.g., using the mean tip velocity, instead of the maximum). Due to the nature of the wing kinematics chosen in this study, the choice for the maximum tip velocity will become obvious.

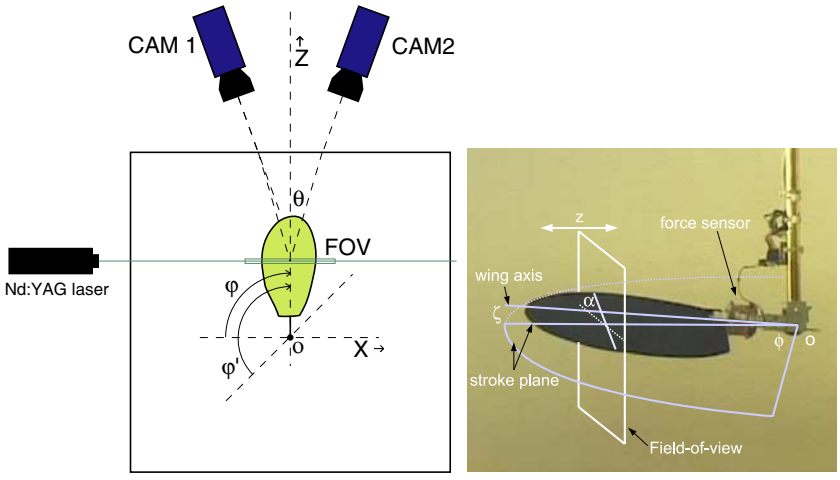

Fig. 2 *Left*: Schematic representation of the dynamically-scaled flapping wing ('Robofly', in *top view*) and the coordinate system with respect to the PIV system. *Right*: Photograph of the arm, force sensor and wing and coordinate system (*side view*). Note that in this photograph a non-transparent wing was used for clarity

will be the period of the flapping cycle. For the fluid dynamics time scale, we use the ratio of the tip velocity (U_{tip}) and the typical chord length of the wing (c). Thus for hovering flight the Strouhal number is of the form $\text{St} = f_{\text{flap}}c/U_{\text{tip}}$. However, it can easily be shown that this Strouhal number scales with the Reynolds number only, as the frequency f_{flap} is proportional to the ratio of a length scale of the wing and the velocity. For the case under consideration, the Strouhal number is 0.06, which means that the flow reaches its quasi-steady state relatively fast compared to the time scale of flapping. As said, the Strouhal number of the scaled model is identical to that of real *Drosophila* ($\text{St} \approx 200 \times 10^{-3}/3.8 = 0.06$).

2.2 Measurement techniques

The local fluid velocity was measured by means of stereoscopic PIV. A 25×25 cm^2 field-of-view was recorded using two Imager Intense cameras ($1{,}376 \times 1{,}024$ pixel resolution, LaVision) equipped with 60-mm lenses (Micro Nikor) on Scheimpflug mounts. They were both placed at an angle of approximately 20–25° with respect to the bisecting line (θ, see Fig. 2). Although a larger bisecting angle would have provided a naturally greater accuracy of the out-of-plane component, we chose a smaller angle for ergonomic convenience. Note that due to the difference in refractive index of air and the oil, the effective angle in the fluid was a few degrees smaller. Such a small angle may lead to a larger uncertainty for the out-of-plane component, compared to the optimal bisecting angle of 45°. An advantage of this relatively small angle was that no significant aberrations of the tracer particle images could be observed due to the non-orthogonal orientation of the cameras with respect to the air/wall/liquid surfaces. Furthermore, the curvature of the focal plane was small compared to the depth-of-field [which was estimated at approximately 3.8 cm for $f/5.6$ and a magnification factor M of 0.044 (Adrian 1997)], so that the entire image was in focus. Liquid-filled prisms were therefore not used. Calibration was performed using a plate with a regular grid of marker dots, distributed over two planes in the z-direction. This allowed an accurate calibration of the out-of-plane component with only a single image for each camera, without the need for displacing the calibration plate. Subsequently, this calibration was iteratively corrected using the disparity map approach (Willert 1997), a processes referred to as 'self-calibration' (Wieneke 2005). This ensured that no errors were introduced by a mismatch in the location of the light sheet and calibration plate. This method of calibration greatly reduces the systematic error in the out-of-plane component (van Doorne et al. 2004). In combination with the ensemble averaging method (described later), this justifies the use of the relatively small separation angle between the cameras.

Silver-coated hollow glass spheres with a mean diameter of 13 μm ('Conduct-o-fil', Potters Industries) were used as tracer material. Due to the high viscosity of the fluid, the particles could accurately follow all motions of the fluid (their response time based on Stokes' drag law was 0.15 μs) and their settling velocity was negligible (terminal velocity 0.7 μm/s).

As light source, a Nd:YAG laser (120 mJ/pulse at 532 nm; New Wave 'Solo') was used; the light sheet was approximately 300 mm high and 2 mm thick; it was always parallel to the chord of the wing at the time of measurement. Images pairs were recorded with a laser pulse delay time of 5,000 or 7,500 μs, depending on the flow pattern; the maximum tracer displacement was always kept below 8 pixels, a value that was chosen by trial-and-error to ensure good PIV results; a higher delay time led to an increased error due to out-of-plane pair loss.[2] For the processing, a three-pass cross-correlation was chosen (one pass at 64×64, two at 32×32 pixels) using a straightforward FFT-based cross-correlation

[2] An a posteriori analysis using the obtained out-of-plane motion made evident that the out-of-plane tracer displacement was always smaller than a quarter of the light sheet thickness for the chosen delay times.

algorithm (DaVis 7.0, LaVision GmbH). Preliminary results indicated that the observed spatial gradients were sufficiently low to justify this choice: the variations of the displacement within one interrogation area were smaller than the typical tracer particle image size, so that broadening of the correlation peak by spatial averaging of the gradients was not an issue (Keane and Adrian 1992). It could thus be assumed that conventional cross-correlation techniques were equally accurate as more sophisticated methods such as image/window deformation (Stanislas et al. 2005), while the latter required significantly more processing time. The number of spurious vectors was comparable for both non-deforming and deforming windows. These spurious vectors were detected in the post-processing step of the final ensemble averaged (described later) vector fields by means of a local median test (Westerweel 1994); a threshold value of 1.5 times the local standard deviation was chosen, and spurious vectors were replaced using bilinear interpolation. Due to the ensemble averaging, typically less than 2% of the vectors needed to be replaced in the ensemble result. For comparison, if individual image pairs were processed (i.e., no ensemble averaging), less than 5% of the vectors needed to be replaced.

In some images reflections of the wing or the gear box were visible, which led to spurious vectors due to parallax effects. These spurious vectors were very distinct, as they were often nearly an order of magnitude larger than the surrounding vectors. The reflections were removed by subtracting an averaged image using 32 recordings. Ideally, an image with only the reflections and no tracer particles should have been used for this. This was nearly impossible, since the reflections were *caused* by scattering of the tracer particles. The averaged image contained the reflections, yet also weak images of the tracer (approximately 1/32 of their mean intensity). This meant that subtracting the average image reduces the image quality somewhat. In regions where no reflections were present, the corrected and uncorrected images gave the same velocity result, which indicated that this method did not introduce any bias to the velocity estimates. In the regions where reflections were present, smooth velocity fields were obtained after the correction. As an alternative approach, each image was pre-processed by means of subtracting a 5×5 median filtered version of the image. The latter acted as a spatial high-pass filter with relatively little smoothing. This method gave similar results, but was computationally more demanding.

2.3 Wing kinematics

Previous studies focusing on force production used kinematics obtained from real freely-flying *Drosophila* using high-speed cameras (Fry et al. 2005). In this study a simplified version of these kinematics was used, as shown in Fig. 3. Different stages in the cycle are represented by the non-dimensional time $\tau \equiv t/T$, with T representing the total cycle duration. From the start (stroke position $\phi = 0°$, $\tau = 0$), the wing rapidly accelerates (at a constant angle-of-attack of 45°) to a constant speed ($\tau = 0.25$). Right before the maximum amplitude $\phi = 180°$, the wing flips around its axis (i.e., 'pronation', at $\tau = 0.5$) and moves in the reverse direction at constant angle-of-attack for the up-stroke ($\tau = 0.75$). Again, before reaching the maximum amplitude, the wing rotates ('supination') and the cycle starts again ($\tau = 1.0$). One full cycle takes 6 s to complete. This simplified kinematics pattern was chosen since it captures many important fluid dynamics phenomena that have been observed using real kinematics and has a comparable force history (Sane and Dickinson 2002). The most important difference is the fact that there is no deviation, i.e., the wing moves in a horizontal plane. In contrast, a real insect wing moves in a slight 'u'-shape, with a typical maximum deviation angle $\zeta = 20°$ (Fry et al. 2003). Additionally, there sometimes is some asymmetry in the up- and down-stroke.

Apart from the differences in kinematics, the deformability of the wing has to be considered. For many insects, passive[3] wing deformation plays an important role (Willmott and Ellington 1997; Combes and Daniel 2003). For hovering fruit flies, this deformation is most significant at the end of the down-stroke. To simplify the study, we used non-flexing wing, although flexing wings may be considered for future studies.

In addition to the simplified flapping pattern the special case of an impulsively-started wing with a constant angle-of-attack ($\alpha = 50°$) was studied. As will be shown later on, this case can be used to investigate two approximations of the rather complex flapping kinematics. The impulsive start (see bottom part of Fig. 3) is comparable to the beginning of the down-stroke part of the flapping cycle, except that the wing continues revolving at a constant angle-of-attack and angular velocity. The wing obviously does not start at the maximum angular velocity: the wing can only be accelerated within mechanical constraints (i.e., forces on the wing, gear box and sensor). In practice, the tip velocity could be described by the following empirical function:

$$u = u_{\max}(1 - \mathrm{e}^{-t/t_c}). \tag{1}$$

The characteristics time (t_c) was of the order of 0.2 s (i.e., the wing reached 63% of its maximum velocity in the first 0.2 s). The maximum amplitude of a 'sweep' was set to 240° to avoid that the wing encountered its own starting vortex. A pause of 12 s was inserted after each 4-s sweep to ensure that each cycle started in (nearly) quiescent fluid.

[3]Passive deformation refers to deformation by aerodynamic or inertial forces, i.e., not due to actual control by muscles.

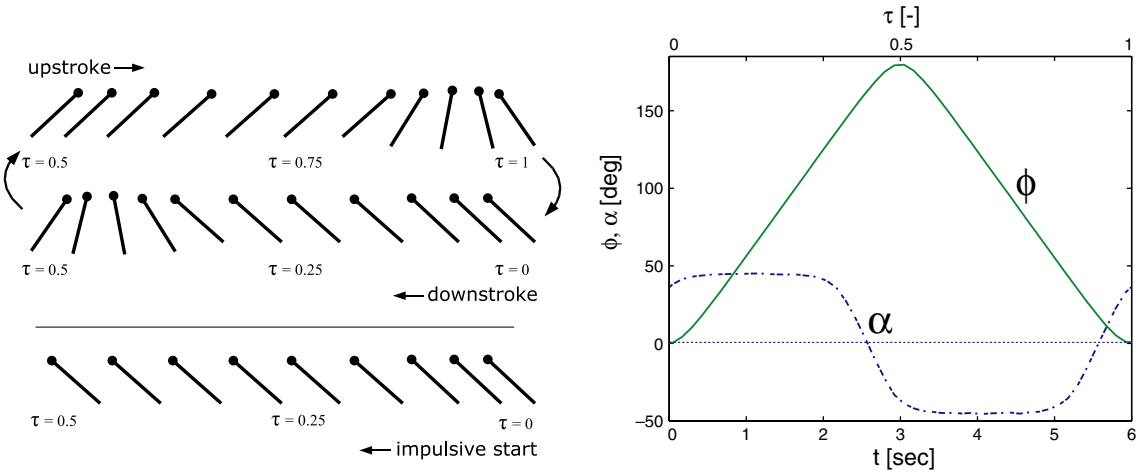

Fig. 3 Wing beat kinematics (see text for details); *top left*: flapping cycle, *bottom left*: impulsive start; *right*: angle-of-attack α and stroke angle ϕ as a function of time for the flapping cycle. Note that for clarity not the actual angle-of-attack is shown here, but rather the angle of the vector *perpendicular* to the wing cord. This avoids 'jumps' due to the change in the wing motion direction

2.4 Data acquisition and reconstruction

At the Reynolds number under consideration, the flow was very repeatable: comparison of repeated PIV results at the same stroke position only differed by small random fluctuations (less than a few percent of the averaged flow). This allowed us to use phase-locked ensemble averaging, which has tremendous advantages. First, the signal-to-noise ratio of the measurements could be significantly enhanced by averaging a number of realizations in the correlation plane domain, in contrast to averaging the actual vector field results. A detailed description of this technique can be found in Meinhart et al. (2000). When the correlation data is averaged for each interrogation spot, the 'true' displacement peak is strongly enhanced, while (uncorrelated) random noise peaks cancel out in the averaging. This also results in a higher accuracy for sub-pixel peak fit than individual realizations. While the PIV results without ensemble averaging were already of good quality, an even better signal-to-noise ratio was desirable for derivatives of the velocity field (e.g., vorticity).

Typically, 35 image pairs were recorded, which allowed analysis using 16×16 interrogation areas if needed, permitting investigation of small flow structures. The choice of the number of image pairs was a compromise between statistical convergence and realistic measurement times for the full set of measurements. For an analysis using 32×32 interrogation areas, it was found that 20–25 images were generally sufficient for convergence of the mean flow (less than 5% change in the mean local velocity). Note that for the flapping case the images of the first three flapping cycles were discarded, to avoid transient 'start-up' effects in the quasi-steady flapping cycle (Birch and Dickinson 2003).

A second, more important advantage of the repeatability is that it allows a complete reconstruction of the flow, because each spanwise position and stroke position can be measured separately (Birch and Dickinson 2001). In order to do so, the PIV system and robotic wing were synchronized and measurements were triggered when the wing is in a specific position. The triggering was done by the PC that controlled the wing motion, which acted as 'master' system. It sent out a pulse at a prescribed stage/angle in the flapping cycle, which triggered the PIV system. This PIV system subsequently triggered the laser and cameras and logged the actual time of measurement. This entire process was very fast compared to the flapping time scale.

Instead of moving the light sheet position and camera, the wing reference frame was rotated and translated with respect to the measurement volume (see Fig. 2: stroke positions ϕ and ϕ' were both recorded at the exact same measurement location, but differed in their starting position. To measure different spanwise positions, the wing reference frame was translated perpendicular to the light sheet, i.e., the spanwise or z-direction). Obviously, this approach eliminated the need for recalibration of the cameras for each measurement. In practice, it was found that the reproducibility of wing location (including spanwise translation) during a series of measurements was very accurate, the differences in observed wing location in the images was never more than a few pixels (i.e., smaller than 1 mm).

The resulting PIV measurements contained typically 87×64 vectors, using interrogation areas of 32×32 with 50% overlap. An example of a spanwise snapshot (averaged over 32 realizations at the same spanwise and stroke position) is given in Fig. 4. The image shows a spanwise plane (at $r = 14$ cm from the center of rotation, i.e., $r/L = 0.56$) of the wing, 0.5 s after an impulsive start. Colors indicate the out-of-plane vorticity component, whereas the contour lines show the out-of-plane velocity (with positive values indicating base-to-tip direction).

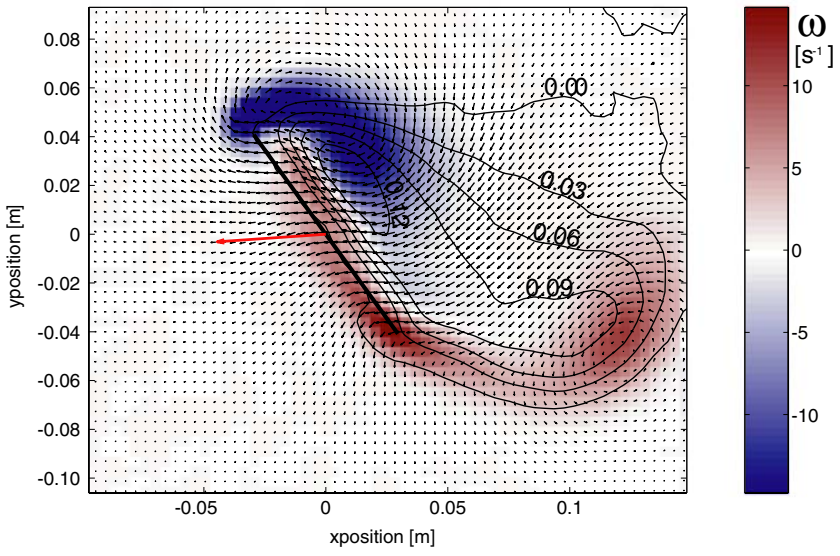

Fig. 4 A snapshot showing the wing (*bold black line*), the fluid velocity field (*black vectors*), the out-of-plane vorticity component (*false colors*), the out-of-plane fluid velocity (*contour lines*, tag units are m/s) and the wing velocity (*red vector*, scale exaggerated by a factor 10). Data taken at $r/L = 0.56$, $\phi = 21°$, impulsive start

At each temporal stroke position, 21 spanwise locations were measured to cover the wing and an area beyond the wing tip. These spanwise locations were spaced 10 mm apart, whereas the in-plane resolution (determined by the PIV vector spacing) was approximately a third of this value. Furthermore, 16 time steps were recorded (typically with a temporal interval of 0.2 s, but they were not necessarily equidistant) to cover one half of the symmetric stroke cycle (from $\tau = 0.25$ to $\tau = 0.75$) and the first stage of the impulsively-starting wing ($\tau = 0.1$ to $\tau = 0.8$, equivalent to $\phi = 0$–$190°$). The choice of the number of spanwise planes and time steps was based on earlier test measurements and was obviously a compromise between resolution and a tractable total measurement time. In total, three large matrices of size $87 \times 64 \times 21$ for 16 time steps were obtained for the velocity components, i.e., in total nearly two million vectors for one half of the flapping cycle. This data was imported and reconstructed in Matlab for further processing. First, the data were corrected for small misalignment errors of the wing reference frame with respect to the measurement coordinate system. This is due to the fact that it is nearly impossible to exactly align the translation stage orientation with the wing axis (see e.g., Fig. 6 for an illustration of the misalignment). This did not introduce an actual measurement error, but was inconvenient for the post-processing stage. A practical example of such an inconvenience was the fact that in subsequent 'slices' of the flow the wing was not exactly at the same location and it was thus difficult to obtain meaningful spanwise derivatives. The data was therefore corrected by rotating the entire data set (measurement locations and velocity orientation). Subsequently, corrected data was obtained by linear interpolation on a grid aligned with the wing axis. These steps are illustrated schematically in Fig. 5. Errors introduced by the interpolation step are expected to be small.

From the corrected data set, the complete gradient tensor ∇u was derived using a central difference scheme. For visualization purposes, the second invariant of the fluid gradient tensor was calculated (Dubief and Delcayre 2000), i.e., $Q \equiv 1/2\,(\Omega_{ij}\Omega_{ij} - S_{ij}S_{ij})$, in which Ω_{ij} and S_{ij} are the antisymmetric and symmetric components of the velocity gradient tensor: $S_{ij} = (1/2)\,(\nabla u + (\nabla u)^t)$ and $\Omega_{ij} = (1/2)\,(\nabla u - (\nabla u)^t)$. The Q-value can be interpreted as a balance between the local swirling strength (Ω) and shear (S). Positive values indicate regions where the swirling motion is dominant; this means that the local value of Q is a useful tool to identify vortical structures, or 'vortex filaments'. Alternatively, the magnitude of the vorticity vector could have been used, but it was found that large shear regions overshadowed the vortical structures that we were interested in. The Q-value effectively removed the contribution from shear, so that these structures became visible. The invariant character of the Q-value makes it a suitable tool for visualization of three-dimensional, curved structures (which cannot be visualized easily by means of isosurfaces of vorticity). Knowledge of the vortex topology (or 'skeleton') will be very beneficial for the understanding of the fluid dynamics involved.

Having the full three-dimensional data allowed a check of the consistency of the data, for instance by testing the zero divergence assumption. For all velocity fields, the absolute value of the divergence ($|\nabla u|$) was calculated and averaged over the three-dimensional field. It was found that this was 1–2% of the maximum gradients in the flow field.

Although the wing location and orientation were prescribed, the actual location was determined a posteriori from the PIV images: a distinct reflection was visible both at the leading and trailing edge of the wing where the laser light sheet entered and left the transparent wing, respectively. For each measurement plane this location was determined, so that the complete

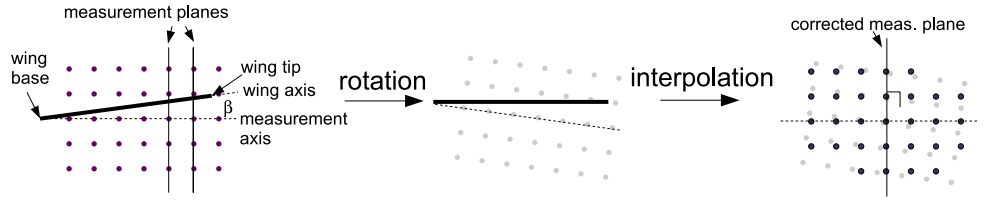

Fig. 5 Schematic representation of the misalignment correction. First, the angle between the wing and measurement axes (β) is determined. Subsequently, the data is rotated over this angle with respect to the intersection of the axes. Finally, the corrected data is obtained by interpolation on a grid aligned with the wing

orientation and location of the wing was known. An example of the reconstructed wing location is shown in Fig. 6. The symbols here denote the sides of the wing as detected from the images. These measurements revealed small undesired movements of the wing, possibly due to backlash in the gear box, belt stretching or flexing of the acrylic wing. The latter was found to be negligible: the wing locations typically fell within 1.5 mm of a plane, approximately the accuracy of the determination of the edges. An example is shown in Fig. 6, where the continuous line is the least-square best fit of a plane through the data. As can been, no deviating trend is visible. If any wing deformation occurred, it was smaller than 1 mm over the entire 250 mm length span. This means that the other two explanations of the wing movement are more likely. Their effects were most evident during the onset of the motion, when there are large changes in the lift and drag forces. During the first 0.1–0.2 s of motion the wing was found to lag and deviate upward a few degrees from the starting position. From the third time step on, the wing settled at an angle-of-attack of 50°, which was 5° higher than the prescribed angle. It was inconvenient that the actual angle could only be determined afterward, yet it did not affect the accuracy or possibilities of the facility. Note that the rotation speed $\mathrm{d}\phi/\mathrm{d}t$ was constant and identical to the prescribed value for $t > 0.2$ s (equivalent to $\tau > 0.033$).

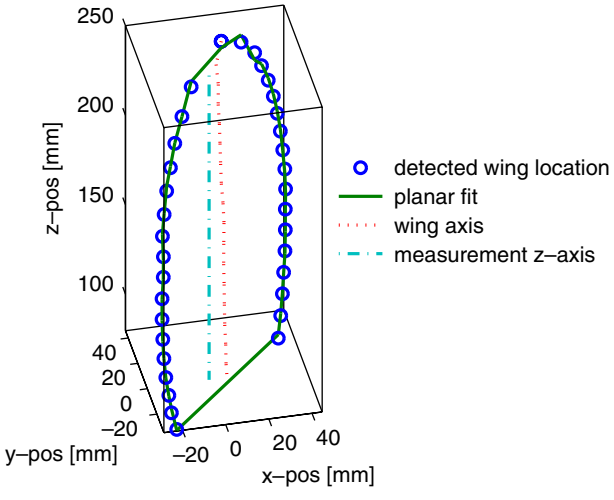

Fig. 6 Example of the detected wing location, fit plane, and measurement and wing axes (see text for details)

3 Results

The experiments using the flapping kinematics and the impulsive start yielded an enormous amount of information. A complete discussion of the fluid mechanical aspects and the biological implications of all these data are beyond the scope of this paper. Here, a few examples are highlighted to demonstrate the richness of the data. In Sect. 3.1, flow visualizations of the impulsively starting wing are shown and discussed. In Sect. 3.2, the quasi-steady state that is observed after a rotation of $\phi > 90°$ is studied. Visualizations from the data obtained using the flapping kinematics are shown in Sect. 3.3. To illustrate the quantitative potential of the data, force predictions using the PIV data set are reported in Sect. 3.4.

3.1 Impulsive-started wing

Visualizations of the initial stages of the impulsively-started wing are shown in Fig. 7. In the same figure, a schematic drawing (top view) of the location of the wing during the three time steps is shown. Note that the visualizations are shown in a frame of reference moving along with the wing; the observer is above the center of rotation and looks down on the wing (i.e., the tip of the wing is at the top of figure). The visualizations are obtained by plotting isosurfaces of the Q-value at each time step. The isosurface is color-coded with the vorticity component in the wing axis direction (ω_z). The red color thus indicates the leading-edge vortex, while the blue denotes the trailing-edge or starting vortex. The figure shows three consecutive time steps ($t = 0.5$, 0.6 and 0.7 s) of an impulsively-started wing at an angle-of-attack of 50°. The Reynolds number, based on maximum chord length and tip velocity is 256. To characterize the formation of the vortices, the dimensionless distance traveled by the wing tip ($F \equiv x/c$, with c the chord length[4]) is also shown. This dimensionless distance is equivalent to the Formation number (Milano and Gharib 2005). Note that here the Formation number is a

[4]The chord length is relatively constant over the span of the wing, except for the tip region, corresponding to roughly the last 10–20% of the wing. For simplicity only one value is used here.

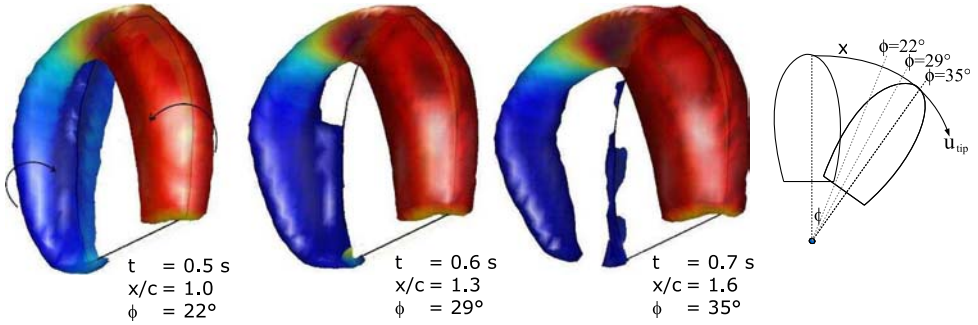

Fig. 7 Flow visualization around an impulsively-started wing at constant angle-of-attack (50°, $Re = 256$) at three consecutive time steps (illustrated schematically at the right-hand side). Visualizations are obtained by plotting an isosurface of the second invariant of the gradient tensor to highlight the core of vortical structures. The false colors on the isosurface denote the contribution from clockwise (*blue*) and counterclockwise (*red*) vorticity in the spanwise direction (as indicated by the *arrows*)

function of spanwise position, unlike in the case of a translating wing.

A clear horseshoe-shaped vortex is evident in the first frame. It is most likely a section of a ring vortex originating around the edges of the wing; the wing extends a bit further toward the point-of-rotation (i.e., bottom of the figure), but this part of the flow cannot be measured due to strong reflections of the gear box. The model wing is truncated at $r = 7$ cm for the force sensor, whereas a real insect wing gradually tapers to the hinge. In the second and third frame, the trailing-edge part of the vortex separates, while the leading-edge part remains mostly attached: only near the tip (approximately the last 30–40% of the span) does it separate and form a tip vortex. The leading-edge vortex will stay attached regardless of the distance the wing travels (see below).

Because the leading-edge vortex is associated with the high lift generated by a wing, its development and stability are of special interest. The aspect of stability will be briefly discussed in Sect. 3.2. For the development stage, the (local) build-up of circulation can be studied in detail using the data set we obtained. The focus here will be on the spanwise component of the circulation (Γ_z), as this is the dominant component of the vector, especially in the early stage. In Fig. 8 the local circulation in the leading- and trailing-edge vortices as a function of the dimensionless path length traveled ($x(r)/c$) is shown. The circulation was determined in each plane by integration of the vorticity contained in the respective vortices. The latter region was defined by setting a threshold value of 25% of the maximum vorticity[5] in each plane. Note that the right-hand figure shows $-\Gamma_z$ to facilitate comparison. On the secondary axis, the circulation is scaled with the wing tip velocity and chord length. The initial points in the graph (near $F = 0$) are most likely influenced by the aforementioned backlash effects of the gearbox. As can be seen in the graph, the data for the LEV collapses in the initial stages, where all vorticity is still bound. It should be noted that the circulation is initially found to be a linear function of spanwise position (i.e., local fluid velocity). The horizontal axis is made dimensionless in Fig. 8, so this is not obvious from the graph. Therefore, the same data of is plotted as a function of spanwise position for different time steps in Fig. 9. As can be seen in this graph, the circulation profiles up to $t = 1.0$ s are linear for a large part of the wing. For $t > 1.6$ *s* the distribution reaches a more or less flat profile (see below). The fact that the distribution changes with spanwise position illustrates the fact that the initial LEV is not a single vortex tube in the 'classical' sense, as the circulation in such a vortex should be constant for each cross-section according to Helmholtz's theorem (Batchelor 1974).

As can be observed in Fig. 8, the spanwise component of circulation in the LEV grows proportional to the Formation number as expected and peaks at a Formation number between 1 and 2, after which it decays somewhat but remains of the same order. On a translating wing, the decay after the peak is generally quite catastrophic (viz. a Von Kármán vortex street, in which the majority of the circulation is shed periodically). Note that the peaks in circulation at all spanwise locations occur at roughly the same Formation number, but in absolute time the regions near the tip reach the maximum significantly earlier than regions near the base. At the trailing-edge, the build-up of circulation occurs at the same rate as at the leading-edge, however a significant part of this vorticity is shed almost immediately (as can also be seen in the visualization shown in Fig. 7). After this initial collapse, the circulation builds up again, but this time it reaches a relatively constant level ($F > 2$). In accordance with Kelvin's theorem, the total sum of local circulation is approximately zero for all frames for $t < 0.7$ s. After this time, three-dimensional (rotation) effects start to dominate and shed vorticity begins leaving the field-of-view.

3.2 Quasi-steady state

If the rotation of the impulsively-started wing continues beyond $\phi = 90°$ (equivalent to approximately four

[5] While this value is rather arbitrary, the results did not change significantly with different threshold values.

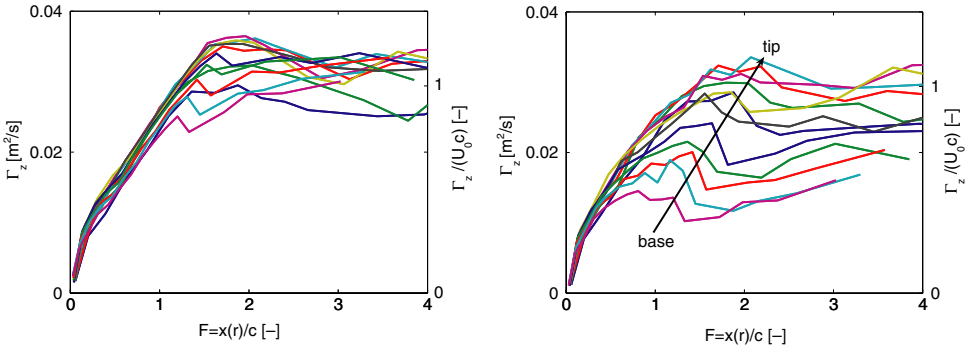

Fig. 8 The spanwise circulation in the leading-edge (*left*) and trailing-edge (*right*) vortices as a function of dimensionless distance traveled (i.e., formation number). The different lines in the graph represent different spanwise planes (from $r/L = 0.40$ to $r/L = 0.84s$, the arrow indicates the order from base to tip). Note that the right-hand figure shows $-\Gamma_z$ for easier comparison

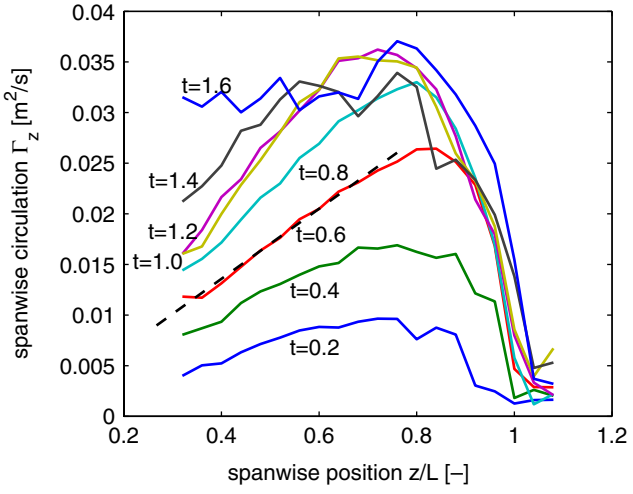

Fig. 9 The spanwise circulation in the LEV as a function of the spanwise position for a number of time steps (indicated by the labels). The *dashed line* illustrates a linear profile, $\Gamma_z = Cz$

chord lengths traveled by the tip), we found that the system approaches a quasi-steady state. The LEV does not grow any further in strength and the flow field remains constant with respect to the wing. The local circulation as shown in Fig. 8 reaches a steady state, which is reflected in the constant measured lift and drag forces on the wing (Dickinson et al. 1999). The initially linear profile of the spanwise circulation in the LEV has changed in a more or less constant distribution (see the data for $t = 1.6$ s in Fig. 9). Visual inspection shows that the flow field still develops somewhat until a rotation angle of $\phi = 180°$, but apparently these changes do not have a great impact on the resulting lift and drag. As the quasi-steady state is already reached at $\phi = 90°$, the flapping cycle (with has a maximum amplitude of $\phi = 180°$) will contain a quasi-steady phase too. This is also illustrated by the relatively small Strouhal number (as reported in Sect. 2.1): the vortex growth is fast compared to the time scale of the flapping cycle.

A visualization of the quasi-steady flow field (at $\phi = 160°$, $x/c \approx 7.5$) is shown in Fig. 10. The figure shows the wing in top view, and the flow has again been visualized using the Q-value. Here the color coding denotes ω_x, the chord-wise vorticity. The visualization clearly shows a large LEV that remains attached to the wing until approximately 60–70% of the wing span. Here, it separates and merges with the tip vortex. The trailing-edge vorticity shows a similar structure, though it remains attached slightly farther toward the tip. The resulting structure sheds from the wing is a pair of counter-rotating vortices (the blue-green and red structures, direction of rotation is indicated by the arrows). In between the two counter-rotating vortices a strong spanwise flow is present (50–75% of the wing tip velocity), as indicated by the bold arrow in the figure.

The magnitude of the circulation contained in the two strands is approximately constant. This can be demonstrated by evaluating the magnitude of circulation $|\Gamma|$ in two slices ($S1$ and $S2$, shown in Fig. 10), one perpendicular to the separated vortex strands ($x = 0.10$ m) and one slicing the attached vortices ($z = 0.13$ m). For the magnitude of circulation in the 'LEV'-structure, we measured

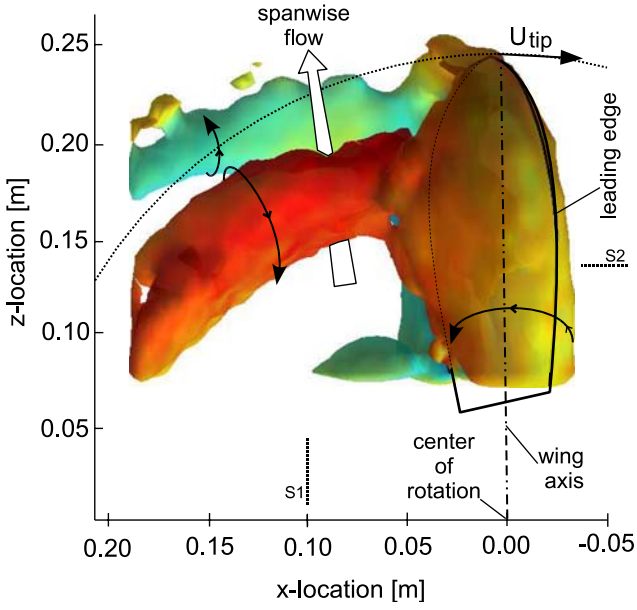

Fig. 10 The quasi-steady flow of a revolving wing at an angle-of-attack of 50°; the viewpoint is from the top, the tip is at the top right of the figure and moves to the right. The colors denote the vorticity in the x-direction (i.e., approximately in the stroke direction), see also the vectors indicating the rotation of the tip vortices. The big vector represents the spanwise flow component

$|\Gamma| = 0.041$ m^2/s and $|\Gamma| = 0.042$ m^2/s for slice 1 and 2, respectively. For the trailing-edge structure, we measured $|\Gamma| = 0.031$ m^2/s and $|\Gamma| = 0.034$ m^2/s, respectively.

In previous studies of flapping flight, the stable leading-edge vortex has received significant attention as the key to the observed enhanced lift (Ellington et al. 1996; Birch and Dickinson 2001). However, at the current high angles-of-attack the production of circulation at the trailing-edge can no longer be ignored. This produces a similar stable structure as the LEV, albeit with a lower circulation (thus the total circulation around the wing is still positive). We feel that the counter-rotating strands of vorticity are a more complete picture than that is often reported in the literature.

For the transition from the early stages as seen in Fig. 7 to the steady-state solution in Fig. 10 the following behavior is observed: the original vortex ring separates at the trailing edge, while the leading-edge part remains attached. This attached structure forms the 'red' tip vortex. The curvature of this structure roughly follows the rotating motion of the wing (see the dashed wing tip trajectory). The second tip vortex (the "green" structure originating in the trailing edge) grows gradually, after the initial shedding of the starting vortex. The radius of curvature is slightly larger, possibly due to the stronger outward spanwise flow at this y-position.

The two strands of vorticity separating from the wing may be key to the stability of the LEV as observed in earlier work. Instead of the conventional alternating shedding of circulation (i.e., a Von Kármán vortex street), there is a continuous 'draining' of circulation that balances the production of circulation at the wing edge. At higher Reynolds numbers (order 10^3), a strong flow through the LEV has been proposed to play this role (Ellington et al. 1996), analogous to the strong core flow in the spiral vortices of delta wing aircraft. At the current Reynolds number there is also a spanwise flow, yet it is spread out in a larger region *behind the wing* (see also Fig. 4). A direct comparison of high and low Reynolds number cases for an identical wing (Birch et al. 2004) observed the same distinct difference. Despite the absence of a strong localized flow, a simple balance of production and transport of circulation in a spanwise plane indicates that the transport ($u_z\,(\partial\Gamma/\partial z)$, obtained in the quasi-steady case) roughly balances the production at the leading edge($(\partial\Gamma/\partial t)$, obtained from the impulsive start data, see Fig. 8) for the attached region. A similar result was recently found in an analytical study by Minotti and Speranza (2005). In the early stage ($t < 1$ s) the spanwise velocity component is negligible, which can explain why the circulation was found to be linearly proportional to the spanwise position during this stage (i.e., there is only production, no transport yet).

3.3 Flapping wing

In Fig. 11, eight consecutive panels are shown during a stroke reversal (from $\tau = 0.76$ to $\tau = 1.25 = 0.25$) in the flapping cycle. The four panels on the left-hand-side represent the final stage of the down-stroke, while the right-hand-side panels are the first stages of the up-stroke (see also Fig. 3). Each panel shows isosurfaces of spanwise vorticity: blue and red colors represent clockwise and counter-clockwise motion, respectively. A single iso-value for the vorticity is used in all panels ($\omega_z = \pm 12$ s^{-1}). The vector in the first and last frame indicates the direction of the wing. The outline of the wing is shown, together with the wing axis (dashed line) and the rotating arm (solid vertical line). The view point is from above, at an angle of 20°, with the tip being closest to the viewer in the bottom of each frame. Note that the view point moves/rotates along with the wing. Also indicated is a schematic representation of the position in the flapping cycle (bold red wing profile).

In frame 1 ($\tau = 0.76$), the wing is in the quasi-steady state as described in the previous section. Clearly, a leading-edge vortex (L1) and a region of counter-rotating vorticity below the wing (T1) can be observed. In the next frame, $\tau = 0.93$, the wing has started to rotate around the wing-axis, while the stroke direction is still the same as in the previous frame. Due to the rotation, the vorticity at the trailing edge (T1) grows significantly.

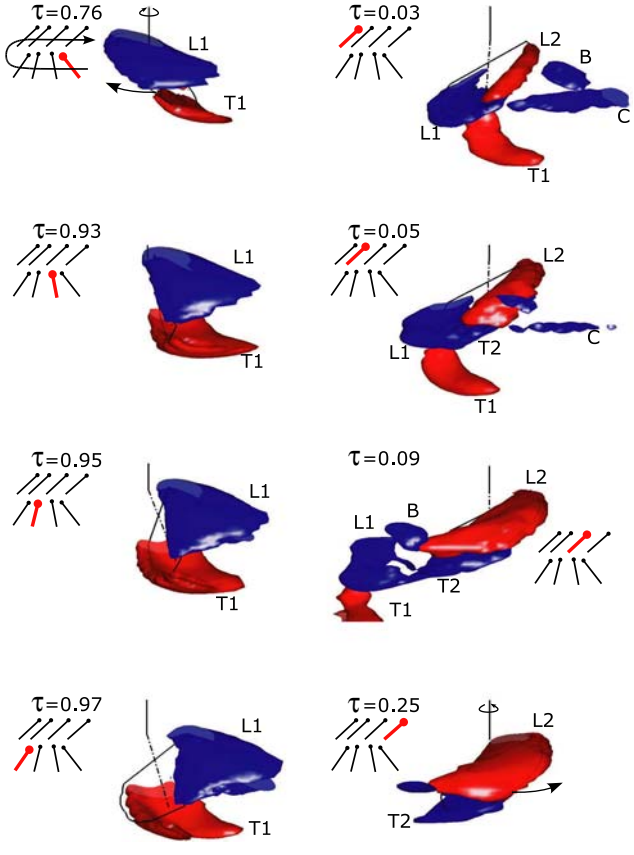

Fig. 11 Composite of eight consecutive visualizations (isovorticity in the spanwise direction) of a stroke reversal (i.e., pronation/supination) in the flapping cycle. See text for description and definition of the labels. The vector in the first and last frame indicates the wing tip velocity

This process continues in the next two frames ($\tau = 0.95$ and $\tau = 0.97$). In the latter, the trailing-edge vorticity detaches from the wing. At this point, the wing has completed the rotation around its axis and begins the down-stroke. The majority of the leading-edge vorticity (L1) gets caught under the wing and is transported toward the trailing edge. This detached leading-edge vorticity merges with the newly developing starting vorticity at the trailing-edge while it is swept along the underside of the wing. Here, it couples with the trailing-edge vorticity that was shed earlier (T1), forming a dipole-like pair of counter-rotating vortices. In frames $\tau = 0.05$ and $\tau = 0.09$ this vortex pair (L1 and T1) can be seen as they are left behind in the wake of the wing, which moves away to the right. In the meantime, a new leading-edge vortex has formed (L2), as well as a region of bound vorticity at the trailing edge (T2). In frame $\tau = 0.25$, another steady-state has been reached, which is a mirrored version of the first frame. The wing then proceeds through the symmetric other half of the stroke cycle (not shown).

Two additional structures can be observed in the panel for $\tau = 0.03$: structure 'B' is a small portion of the initial LEV (L1), which is not trapped under the wing like the rest, but rather passes *over* the wing as the wing moves through its own wake. The structure labeled 'C' is either a structure that was initially outside of the field-of-view ($z < 0.07$ m), e.g., the continuation of structure T1. Alternatively, it may be formed due to a roll-up of a relatively weak vortex sheet.

The shedding of a pair of counter-rotating vortices as evident in frames $\tau = 0.05$–0.09 has also been observed in a two-dimensional numerical study by Wang (2000). In that study, the wing moved in an inclined plane (versus the horizontal plane in this study), so that the momentum carried by the vortex pair contributed to lift. Here, this effect is negligible and only drag (i.e., horizontal force) is generated. Additional experiments *with* deviation are needed to see if this vortex pair shedding plays a role in real insect kinematics.

3.4 Force prediction

To demonstrate that the data set can also be used for quantitative analyses, the force acting on the wing was estimated from the velocity fields. Using the force sensor mounted at the base of the wing, this force could also be determined independently as verification.

There are several approaches to calculate the force on an immersed object from the surround velocity field. Some techniques use exact relationships linking the (transient) vorticity field to forces (Noca et al. 1999). Alternatively, one can use the momentum contained in the vortex rings produced by the object to find the mean force during a cycle (Rayner 1979; Spedding et al. 1984; Dabiri 2005). The drawback of the latter is that some transient forces, especially added-mass terms, are not easily accounted for (Dabiri 2006). In this paper, we chose to use a very straightforward, exact equation as derived by Wu (1981):

$$F = -\frac{1}{2}\rho\frac{\mathrm{d}\gamma}{\mathrm{d}t} + \rho\frac{\mathrm{d}}{\mathrm{d}t}\int_R u\mathrm{d}R \quad \text{with} \quad \gamma = \int_Z \omega \times r\mathrm{d}r. \qquad (2)$$

The first term in Eq. 2 accounts for the effect of the flow field under consideration (i.e., enclosed in volume Z) on an immersed object. This is expressed in the derivative of the first moment of vorticity, γ. The second term accounts for the change in momentum of the displaced fluid by the object (enclosed in volume R) itself. Since the wing is thin and accelerations are negligible for the case under consideration, the latter is expected to be relatively small compared to the fluid-induced forces.

It should be noted that this method predicts the total forces, regardless of the physical 'mechanism'. It has become common to differentiate several mechanisms in flapping flight aerodynamics, such as 'rotational lift', 'wake capturing' and 'added-mass'. These were mainly introduced to improve the results from quasi-steady models, which systematically under-predicted the lift and drag forces (Sane and Dickinson 2002). Since all these effects are present in the transient flow field, there are inherently taken into account by Eq. 2 and no additional correction terms are needed.

In this test case, the data from the impulsively-started wing were used. Figure 12 shows the horizontal and vertical forces acting on the wing, as predicted using the PIV data and Eq. 2, as well as those measured by the force sensor. As can be seen in the graph, the overall agreement is reasonable, although the forces are systematically under-predicted by 10–20%. A possible explanation for this discrepancy is the fact that the wing

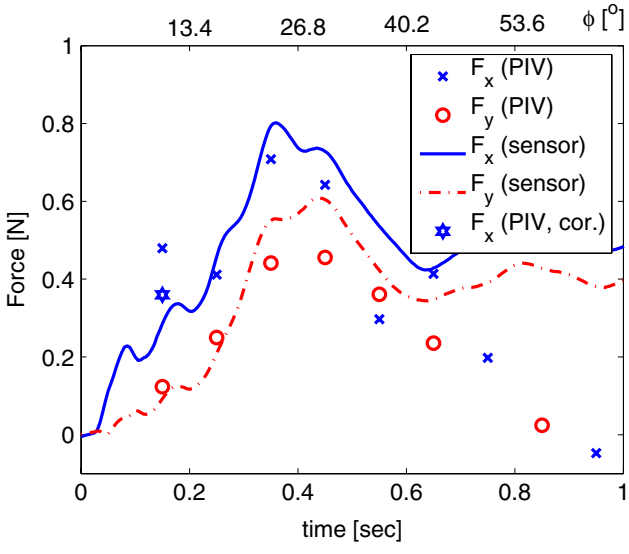

Fig. 12 The measured (*lines*) and predicted (*symbols*) horizontal and vertical forces acting on the impulsively-started wing. *Continuous line* and *crosses* represent the horizontal forces, *dashed line* and *circles* represent vertical forces. The *star* indicates the corrected horizontal force (see text)

extends somewhat beyond the measurement volume: in the final 2 cm near the base, the reflections were too strong to obtain PIV results (due to camera overexposure). If we assume that the force production scales proportional to the spanwise velocity, which itself scales linearly with radial position, this can account for approximately 4–5% of the total force. The remainder can most likely be contributed to the fact that the initial stages of the flow are not as well resolved temporally as is required. Note that the under-prediction of the forces cannot be explained by a missing 'mechanism' such as added-mass, for the reason explained earlier.

There are likely explanations for the data points that deviate significantly (apart from the systematic under-prediction). For the first point, at $t = 0.15$ s, the second integral in Eq. 2 was neglected, even though this is the stage when the wing still accelerates (see also Eq. 1). Therefore, especially the horizontal (drag) force is poorly predicted. When the contribution of the displaced fluid integral is taken into account, the agreement is better (as indicated by the star (✡) in Fig. 12). Furthermore, the predictions for $t > 0.65$ s are all quite poor. This can be explained by the fact that at this moment vorticity starts 'leaking' from the measurement volume. In earlier stages, all vorticity was confined to the center of the measurement volume. Noca et al. (1999) have developed methods to account for the vorticity flux through the measurement boundaries (by expressing equations similar to Eq. 2 solely in terms of derivatives on a control surface, rather than an 'infinite' measurement volume). An implementation of these equations will likely improve the predictions for $t > 0.65$ s. Needless to say, the flapping case will also require this more sophisticated treatment to get meaningful force predictions.

Regardless of these shortcomings in the technique, force prediction from PIV velocity fields are very useful for linking the observed lift to the unsteady fluid dynamics phenomena. For instance, the characteristic peak in the forces ($t = 0.04$–0.05 s) occurs during the stage where vorticity is generated. The maximum occurs immediately before the trailing-edge (starting) vortex separates. The circulation in the leading edge vortex continues to grow, so an increase would be expected. However, the starting vortex separates and moves away from the wing, leading to a significant drop in the forces. Similar results were obtained earlier by Birch and Dickinson (2003). However, in their publication only the qualitative trends of the sectional lift and drag were considered, while in the present work actual forces are reported and compared.

Since all three velocity components are known from the stereoscopic measurements, the effect of measuring only one component of vorticity (as in standard two-component PIV) can be studied. The most commonly used aerodynamic theories are based on infinitely-long (i.e., two-dimensional) wings, so the spanwise circulation is usually the only component that is considered. While this is generally a good approximation, as this spanwise circulation is dominant for the lift and drag production, it is interesting to see to what extent the other two components play a role. To this purpose, the force prediction using Eq. 2 was repeated with ω_x and ω_y set to zero. This analysis yielded a systematic under-prediction of 8–10% for the lift and drag forces compared to the case using the full vorticity. This result can be understood by considering Fig. 7: if ω_x and ω_y are neglected, only the contribution from the red and blue parts (ω_z positive and negative, respectively) of the vortical structure surrounding the wing are taken into account, ignoring the yellow-green section of the structure (where $\omega_z \approx 0$). In this case the effect was not so significant, but with a decreasing aspect ratio of a wing the relative contributions of ω_x and ω_y will become more important.

4 Conclusions

Using a phase-locked stereoscopic PIV system the complete three-dimensional, time-resolved velocity field around a flapping wing has been measured for the first time. Two cases were reported: an impulsively-starting wing and a simplified flapping pattern. Both cases can be characterized by a Reynolds number comparable to that of a real *Drosophila*. Even the simplified flapping pattern generated very complex, interacting structures. The data from the impulsively-started wing was used to highlight two regimes that were observed in the flapping cycle: the initial stage with large changes in local circulation and a quasi-steady state that set in at $\phi > 90°$.

The initial stage of the impulsively-started wing is important for an understanding of the dynamics of the leading-edge and starting vortex. In this stage, there is no significant spanwise flow and the growth of the circulation is linearly proportional to the locally traveled distance of the wing. In the quasi-steady stage there is a significant spanwise flow behind the wing (and thus not localized in the LEV core). This flow can be the key to the observed stability of the flow field, as it drains circulation from the wing and can therefore balance the production at the leading edge. The observed flow field shows two stable counter-rotating vortical structures, which remain attached until 60–70% of the wing span. This observation refines the picture that is reported in a number of previous studies (which relied mainly on flow visualization), where only a single leading-edge vortex was observed.

Apart from flow visualizations, it was shown that the data could also be used for more quantitative analyses. As an example, the data set of the impulsively-started wing was used to predict the forces acting on the wing. While there is still significant room for improvement (mainly in the temporal resolution and a solution for the vorticity flux through the measurement boundaries), the results of the predictions compare reasonably well with separate measurements using a force sensor.

Acknowledgments Support from The Netherlands Organization for Scientific Research (NWO) in the form of a 'Talent' Fellowship is gratefully acknowledged (CP). Additional support was provided by a grant from the National Science Foundation, the Packard Foundation and the Office of Naval Research (MHD).

References

Adrian R (1997) Dynamic ranges of velocity and spatial resolution of particle image velocimetry. Meas Sci Technol 8:1393–1398

Batchelor GK (1974) An introduction to fluid dynamics. Cambridge University Press, Cambridge

Birch JM, Dickinson MH (2001) Spanwise flow and the attachment of the leading-edge vortex on insect wings. Nature 412:729–733

Birch JM, Dickinson MH (2003) The influence of wing–wake interactions on the production of aerodynamic forces in flapping flight. J Exp Biol 206:2257–2272

Birch JM, Dickson WB, Dickinson MH (2004) Force production and flow structure of the leading edge vortex on flapping wings at high and low Reynolds numbers. J Exp Biol 207(7):1063–1072

Bomphrey RJ, Lawson NJ, Harding NJ, Taylor GK, Thomas ALR (2005) The aerodynamics of *Manduca sexta*: digital particle image velocimetry analysis of the leading-edge vortex. J Exp Biol 208:1079–1094

Bomphrey RJ, Taylor GK, Lawson NJ, Thomas ALR (2006a) Digital particle image velocimetry measurements of the downwash behind a desert locust *Schistocerca gregaria*. J R Soc Interface 3(7):311–317

Bomphrey RJ, Lawson NJ, Taylor GK, Thomas ALR (2006b) Application of digital particle image velocimetry to insect aerodynamics: measurement of the leading-edge vortex and wake of a Hawkmoth. Exp Fluids 40(4):546–554

Combes SA, Daniel TL (2003) Flexural stiffness in insect wings. II. spatial distribution and dynamic wing bending. J Exp Biol 206:2989–2997

Dabiri JO (2005) On the estimation of swimming and flying forces from wake measurements. J Exp Biol 208:3519–3532

Dabiri JO (2006) Note on the induced lagrangian drift and added-mass of a vortex. J Fluid Mech 547:105–113

Dickinson MH, Lehmann F-O, Sane SP (1999) Wing rotation and the aerodynamic basis of insect flight. Science 284(5422):1954–1960

van Doorne CWH, Westerweel J, Nieuwstadt FTM (2004) Measurement uncertainty of stereoscopiv-piv for flow with large out-of-plane motion. In: Proceedings of the EUROPIV 2 workshop held in Zaragoza, Spain, March 31–April 1, 2003, pp 213–227

Dubief Y, Delcayre F (2000) On coherent-vortex identification in turbulence. J Turbulence 1:1–22

Ellington CP, Van den Berg C, Willmott AP, Thomas ALR (1996) Leading-edge vortices in insect flight. Nature 384:626–630

Fry SN, Sayaman R, Dickinson MH (2003) The aerodynamics of free-flight maneuvers in *Drosophila*. Science 300(5618):495–498

Fry SN, Sayaman R, Dickinson MH (2005) The aerodynamics of hovering flight in *Drosophila*. J Exp Biol 208(12):2303–2318

Hedenström A, Rosén M, Spedding GR (2006) Vortex wakes generated by robins erithacus rubecula during free flight in a wind tunnel. J R Soc Interface 3(7):263–276

Keane RD, Adrian RJ (1992) Theory of cross-correlation analysis of PIV analysis. Appl Sci Res 49:191–215

Meinhart CD, Wereley ST, Santiago JG (2000) A PIV algorithm for estimating time-averaged velocity fields. J Fluids Eng 122:285–289

Milano M, Gharib M (2005) Uncovering the physics of flapping flat plates with artificial evolution. J Fluid Mech 534:403–409

Minotti FO, Speranza E (2005) Leading-edge vortex stability in insect wings. Phys Rev E 71:051908

Noca F, Shiels D, Jeon D (1999) A comparison of methods for evaluating time-dependent fluid dynamic forces on bodies, using only velocity fields and their derivatives. J Fluids Struct 13(5):551–578

Rayner JMV (1979) A vortex theory of animal flight .1. Vortex wake of a hovering animal. J Fluids Mech 91:697–730

Sane SP, Dickinson MH (2002) The aerodynamic effects of wing rotation and a revised quasi-steady model of flapping flight. J Exp Biol 205:1087–1096

Spedding GR, Rayner JMV, Pennycuick CJ (1984) Momentum and energy in the wake of a pigeon (Columba livia) in slow flight. J Exp Biol 111:81–102

Spedding GR, Rosén M, Hedenström A (2003) A family of vortex wakes generated by a thrush nightingale in free flight in a wind tunnel over its entire natural range of flight speeds. J Exp Biol 206:2313–2344

Stanislas M, Okamoto K, Kähler CJ, Westerweel J (2005) Main results of the second international PIV challenge. Exp Fluids 39:170–191

Taylor GK, Nudds RL, Thomas ALR (2003) Flying and swimming animals cruise at a strouhal number tuned for high power efficiency. Nature 425:707–711

Usherwood JR, Ellington CP (2002) The aerodynamics of revolving wings—I. model hawkmoth wings. J Exp Biol 205(11):1547–1564

Von Ellenrieder KD, Parker K, Soria J (2003) Flow structures behind a heaving and pitching finite-span wing. J Fluid Mech 490:129–138

Wang ZJ (2000) Two dimensional mechanism for insect hovering. Phys Rev Lett 85(10):2216–2219

Wang ZJ (2005) Dissecting insect flight. Annu Rev Fluid Mech 37:183–210

Westerweel J (1994) Efficient detection of spurious vectors in particle image velocimetry data. Exp Fluids 16:236–247

Wieneke B (2005) Stereo-PIV using self-calibration on particle images. Exp Fluids 39:267–280

Willert CE (1997) Stereoscopic digital particle image velocimetry for application in wind tunnel flows. Meas Sci Technol 8:1465–1479

Willmott AP, Ellington CP (1997) The mechanics of flight in the hawkmoth *Manduca sexta*. I. kinematics of hovering and forward flight. J Exp Biol 200:2705–2722

Wu JC (1981) Theory for aerodynamic florce and moment in viscous flows. AIAA J 19(4):432–441